Materials Systems and Processes for Three Dimensional Micro- and Nanoscale Fabrication and Lithography, S. M. Kuebler and V. T. Milam, Eds, Materials Research Society, Vol. 1179E, 1179-BB08-02 (2009)

Thermocapillary Patterning of Nanoscale Polymer Films

Mathias Dietzel and Sandra M. Troian
Dept. of Applied Physics, Laboratory of Interfacial & Small Scale Transport,
California Institute of Technology, 1200 E California Blvd, MC 128-95, Pasadena, CA 91125

ABSTRACT

We investigate a novel method for non-contact patterning of molten nanoscale polymer films based on thermocapillary modulation by an imposed temperature distribution. The induced variations in polymer surface tension are used to shape and mold nanofilms into 3D structures, which rapidly solidify when cooled to room temperature. Numerical simulations of the evolving free surface during the flow process illustrate how this technique is used to fabricate in one process step arrays of nanostructures with disparate heights and spacing. These results provide guidelines for controlling proximity effects to achieve pattern replication with high fidelity.

INTRODUCTION

Conventional photolithographic patterning techniques are intrinsically costly and time consuming since step-and-repeat processes are required for alignment of substrate registration marks with photomask features and for deposition and removal of photoresist layers. Resolution limits, however, have achieved the once unimaginable range of sub-100 nm. In parallel with improvements to this technology are efforts focusing on less costly, large area, lower resolution techniques capable of extension to flexible substrates for fabrication of polymeric masks as well as optoelectronic, photonic and biofluidic components. Some of these unconventional patterning techniques include ink-jetting [1], gravure printing [2], direct-write [3], micro-molding [4] and molten silicon imprinting [5]. While these techniques are more easily adaptable to a host of new materials and complex layouts, they too often require multiple etching treatments in order to create 3D structures, which also ultimately imbue final structures with significant surface roughness. These techniques also require multiple layers to be deposited in order to generate 3D structures of variable height and shape from sequential overlays of 2D patterns. Our interest in inexpensive production of masks and structures of nanoscale films has led us to investigate a novel non-contact, intrinsically 3D technique based on thermal modulation of the surface tension of a molten polymer nanofilm. Imposed thermal variations along the film surface generate thermocapillary stresses which are used to elongate or depress selective regions of the film to create desired 3D nanostructures. For the polymer materials of interest, namely polystyrene (PS) and poly(methyl methacrylate) (PMMA), the polymer melt flows toward cooler and away from warmer targets.

We recently launched an effort to understand the physical mechanism leading to film patterning in a number of experiments conducted by several groups during the past decade [6-10]. In these experiments, it was shown that a nanoscale molten polymer film subject to an ultra large transverse gradient undergoes spontaneous formation to self-assembling nanopillar arrays. In brief, a spun cast film of PS or PMMA of thickness h_o (80-130 nm) is placed on a hot silicon wafer at a temperature T_2 held above the polymer glass transition (approx. 130-170°C) during processing. A second cooled parallel wafer held at temperature T_1 is situated a distance d_o (100-600 nm) above the first, leaving a critical air gap of dimension d_o - h_o. Although the

temperature drop $\Delta T=T_2 - T_1$ across the two wafers is rather small (10-50°C), the narrow gap size establishes a very large thermal gradient of order 10^6-10^8 °C/cm. The initial flat film spontaneously self-assembles into a large array of nanopillars with in-plane hexagonal symmetry and mean spacing of order 1-10 μm. Upon removal of the thermal gradient, the nanopillars rapidly solidify in place forming well ordered solid arrays. In previous work [11], we have challenged the current explanation for nanopillar formation, which is based on a phenomenological radiation pressure induced by interfacial reflections of acoustic phonons. We have argued instead that thermocapillary stresses play a critical if not dominant role in pillar formation. A linear stability analysis of the governing interface equation reveals good agreement between the mean pillar spacing measured in experiment and predictions for the most unstable wavelength λ_{max}, which determines the nanopillar array pitch. In this work, we examine the influence of a patterned upper wafer on the film shaping process. A cross-sectional view of the assembly corresponding to the numerical simulations in this current study is shown in Figure 1. The cooler wafer contains numerous protrusions whose surface temperature is held fixed at T_1. We investigate by numerical simulation wave interference effects during the formation process due to the proximity of adjacent structure formation and study the influence of the imposed lateral feature size on the number and shape of peaks formed.

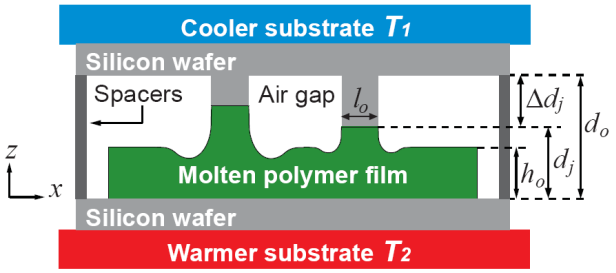

Figure 1 Schematic diagram of experimental setup for nanopillar formation. Upper wafer contains protruding elements (labeled by index j) of diameter l_o and depth d_o–d_j. For the numerical simulations of the formation process in this study, h_o=100 nm, d_o=285 nm and $\Delta T= T_2 - T_1$ = 170°C-124°C = 46°C. All remaining variables and material properties are given in the text.

THEORETICAL MODEL

The derivation for the velocity fields and interface equation corresponding to the flow within the thin polymer film due to thermal modulation of the air/polymer surface tension is rather lengthy and therefore not reproduced here. The interested reader is referred to Ref. 11 for details. The most notable assumptions of the theoretical model consistent with experiment are (i) the polymer film is modeled as a simple Newtonian fluid, since the shear rates are much less than 1 $\sec^{-1}$, and its viscosity is assumed constant over the range ΔT examined, (ii) the fluid dynamics and heat transfer processes are well approximated by the slender gap limit [12] for which $\varepsilon^2=(h_o/ l_o)^2<<1$ and $\varepsilon Re <<1$, where Re is the Reynolds number based on the initial film height h_o, and (iii) the energy equations for the gas and polymer melt reduce to 1D conduction equations along the z-axis. The variation in temperature gradient along the film interface generates a variable tangential shear stress which establishes the boundary condition at the (dimensionless) free surface $Z=H(X,Y,\tau)$. The resulting evolution equation for the dimensionless film height $H(X,Y,\tau) =h(x,y,t)/h_o$ is given by:

$$\frac{\partial H}{\partial \tau} + \nabla_{\parallel} \cdot \left(\frac{\kappa Ma H^2}{2\left[D + (\kappa - 1) H \right]^2} \left(D \nabla_{\parallel} H - H \nabla_{\parallel} D \right) + \frac{H^3}{3\, Ca} \nabla_{\parallel}^3 H \right) = 0 \,. \qquad (1)$$

Here, the dimensionless variables are defined by $(X,Y,Z) = (x/l_o, y/l_o, z/h_o)$ where l_o is the lateral feature size shown in Figure 1 (which in this study is held constant for protrusions within a particular array), $\nabla_{\|} = (\partial/\partial X, \partial/\partial Y)$, $[H, D_o, D, D_j, \Delta D_j] = [h(x,y,t)/h_o, d_o/h_o, d(x,y)/h_o, d_j/h_o, \Delta d_j/h_o]$ where $D(X,Y)$ defines the surface topology of the upper wafer, $\tau = t\, u_c/l_o$ where t is real time, $\kappa = k_{\text{air}}/k_{\text{polymer}}$ is the ratio of thermal conductivities, $Ma = \varepsilon\gamma_T \Delta T/(\eta u_c)$ is a modified Marangoni number and $Ca = \eta u_c/(\gamma\varepsilon^3)$ the modified capillary number. Additionally, $\gamma_T = |d\gamma/dT|$ denotes the variation in surface tension with temperature, $\Delta T = T_2 - T_1$, $\eta = \eta(T_2)$ is the polymer viscosity and $u_c = (4\pi)^2 \varepsilon\gamma\, h_o^2/(3\eta\lambda_{max}^2)$ is the characteristic lateral flow speed established by thermocapillary flow. Material parameters which are temperature dependent are also typically referenced to the temperature T_2. The length scale λ_{max} defines the wavelength of the fastest growing mode computed from linear stability analysis [11], which corresponds to the average pillar separation distance for an initially flat film which undergoes pillar formation in between two flat, parallel plates:

$$\lambda_{max} = 2\pi h_o \sqrt{4\gamma h_o / (3\gamma_T \Delta T \kappa d_o)}\,(d_o/h_o + \kappa - 1). \qquad (2)$$

As evident from Eq. (1), the evolving film thickness $H(X,Y,\tau)$ is controlled by the competition between thermocapillary terms (preceded by the coefficient Ma), which drive the flow toward cooler protrusions, and the capillary term (preceded by the coefficient Ca^{-1}), which represses formation of additional film surface area. Gravitational forces are negligibly small for the nanoscale films of interest. In what follows, we focus on numerical simulations in which the topology of the top wafer is described by an array of protrusions labeled by index j of lateral extent l_o and depth $D(X,Y) = D_o - \Delta D_j\, F(X,Y)$ where $F(X,Y) = \{1 - \tanh[c(2\xi/l_o - 1)]\}/2$ and c controls the side-wall slope of a protruding element, set to the value 10 in these studies. For the case of a single extended ridge, $\xi = |X|$; for the example of cylindrical arrays discussed next, $\xi = [(X-X_{o,j})^2 + (Y-Y_{o,j})^2]^{1/2}$, where $(X_{o,j}, Y_{o,j})$ denotes the cylinder face midpoint when viewed from above. We note that Eq.(1) is only valid up until the moment when the polymer film first makes contact with a protruding element. Polymer spreading along the protrusion surface requires additional specification of the dynamics of moving contact lines, which is outside the scope of this work.

DISCUSSION

We have conducted finite element simulations [13] of Eq. (1) for two types of wafer topology to gain insight into proximity effects arising from wave interference during pattern evolution. For all studies presented except where explicitly noted, the following parameters were held fixed: h_o=100 nm, d_o=285 nm, T_2=170°C and T_1=124°C. The material constants correspond to those of PS quoted in the literature: γ= 0.0315 N/m and $\gamma_T = 0.0885 \cdot 10^{-3}$ N/m-°C (at 180°C [14]), $\eta = 2.5 \cdot 10^5$ Pa-s (at 170 °C [15]) and κ=0.277 (at 170 °C [16,17]). For the configuration examined in Figure 2, the top wafer is patterned into a square array of four cylinders of diameter l_o=1 μm, which measure in depth ΔD_j (j = 1–4) = 1.25, 1.0, 0.75 and 0.50. In this case, u_c=2.84 nm/s, λ_{max} = 4.83 μm, Ma = 5.73 and Ca = 2.25. Shown in the figure are cross-sectional views along the perimeter length S for pillar spacing ΔS = 2, 3, 4 and 5 (measured in units of l_o) for four times τ ranging from 0 to 0.145; the final time corresponds to contact of the polymer melt with the longest protrusion. The inset in (b) shows 3D images of the evolving film at the prescribed times for pillar spacing ΔS=3. The metric bar shown in (c) provides a comparison of the spacing ΔS to

the dimensionless wavelength λ_{max}/l_o=4.83. The color inset in (d) displays the variation in polymer surface temperature $\Theta(Z=H) = (T_{z=h}-T_1)/(T_2-T_1)$ at the specified time for pillar spacing ΔS=5. These results indicate that the time required to contact the longest protrusion is rather insensitive to ΔS; however, the longest protrusion generates the most significant film deformation, both vertically and horizontally, since the local thermal gradients are larger. The material required to grow a peak flows from its vicinity, a process which depletes fluid from the surrounding area and produces the characteristic dips observed on either side of the main peak. For the shapes shown in Figure 2(a) – (d), the lateral extent of film deformation beneath the longest protrusion is approximately $4l_o$. Consequently, neighboring waveforms undergo interference for cylinder spacings less than this value, as observed in Figures 2(a) and (b). Constructive interference between neighboring perturbations also leads to steeper depressions, as shown in Figure 2(a). The amplitude and lateral extent of these oscillatory sidewaves depends on the time required for the main peak to reach the protruding surface; therefore, good temporal control is ultimately required to affix desired shapes.

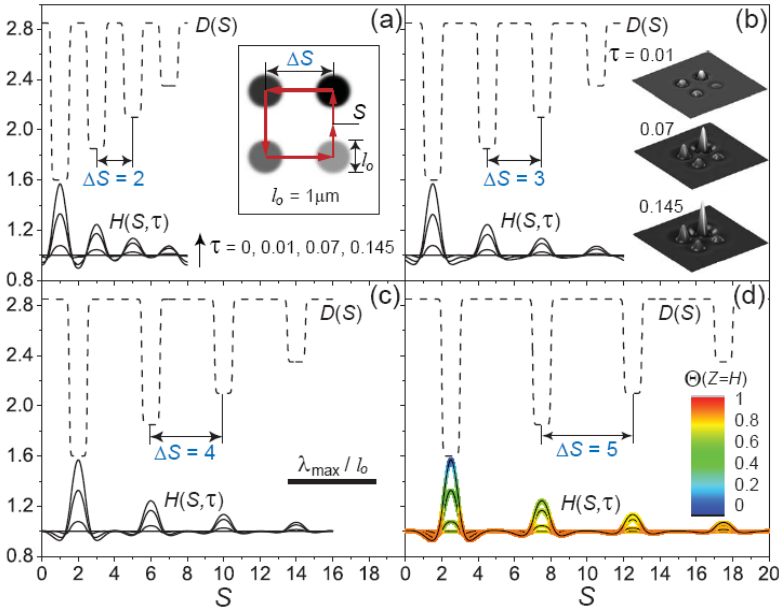

Figure 2 Plots of the film thickness $H(S,\tau)$ as a function of perimeter distance S (measured in counterclockwise fashion) as a function of time τ= 0.0, 0.01, 0.07 and 0.145 for a square array of cylindrical protrusions of diameter l_o=1 μm and decreasing size 1.25, 1.0, 0.75 and 0.5 (in units of h_o), separated by an equal distance (a) ΔS=2, (b) ΔS=3, (c) ΔS=4 and (d) ΔS=5.

These results, while not exhaustive, illustrate the advantages of using substrate preforms to enhance or depress selective regions of a polymer film within a single processing run. By contrast, conventional patterning by photolithography requires many sequential steps in order to fabricate structures of varying height. The simulations also reveal that for the polymer materials of interest and temperature differences used, the pillar formation process is surprisingly rapid; for the cases shown, the tallest peak contacts the upper protrusion in less than a minute. This fast response is due to the fact that the surface thermal gradient is continuously increasing as the film approaches the upper plate, as depicted by the colored thermal profiles shown in Figure 2(d), which leads to ever faster film deformation.

The study shown in Figure 3 demonstrates more clearly the influence on film shape caused by an imposed feature size smaller and larger than the hydrodynamic length scale λ_{max} . Shown in Figure 3(a) is a cross-sectional view of the film shape generated by a single protrusion of depth 50 nm resembling an extended ridge with a width at half-maximum set either to 4 or 5 μm. For comparison, the corresponding instability wavelength if the wafers were flat is λ_{max}= 4.83 μm. For the smaller ridge width, the film develops a single peak centered beneath the protrusion. For the larger ridge width, two sharp peaks develop beneath the corners of the ridge. Corresponding

3D images of the film shape are shown in Figure 3(b). For these runs, Ma= 5.73, Ca=36.0 for the smaller width (u_c = 0.71 nm/s) and Ca=56.3 for the larger width (u_c = 0.57 nm/s). Inspection of Eq. (1) reveals that the stabilizing effect of capillary forces is weakened for the wider profile, which enables the formation of two peaks. As also shown in Figure 3(b), the narrow protrusion allows the formation of a central peak with little undulation along the Y-axis within the time interval needed for the polymer to contact the protrusion. In contrast, the wider protrusion generates an instability along the peak backbones upon approach to the protruding surface. If in Eq. (2) we substitute for d_o the local gap distance between the bottom substrate and bottom of the ridge i.e. d_f=235 nm, then λ_{max} = 4.07 μm or likewise, λ_{max} /l_o =0.814, which closely approximates the wavelength observed for this backbone instability. We are investigating whether this secondary instability develops in response to the fact that the wider ridge width, which exceeds the value λ_{max} and therefore allows formation of two peaks, produces spikes of higher curvature possibly also subject to a Rayleigh-like instability in addition to thermocapillary instability.

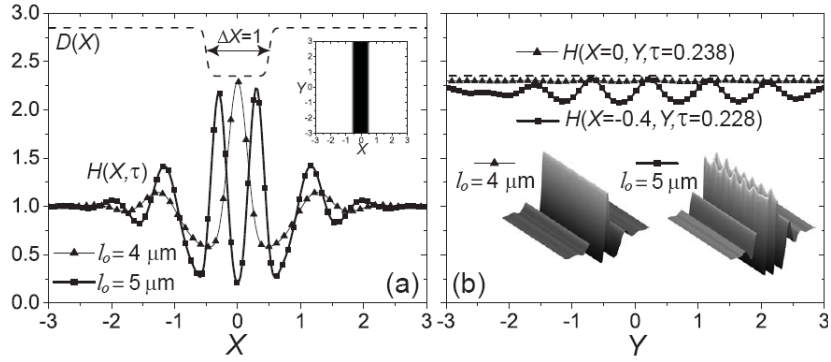

Figure 3 Plots of film shapes induced by a top wafer patterned with a single extended protrusion resembling a ridge of width 4 or 5 μm. (a) Cross-sectional view of film surfaces along the X-axis. (b) Cross-sectional view of film surfaces along the Y-axis. Remaining parameter values are given in the text.

Waveform distortion can be minimized by placing protrusions in close proximity to the film surface. Shown in Figure 4 is an example of a protrusion similar in shape to the wider ridge in Figure 3 but for different processing parameters where h_o = 500 μm and d_o = 2 μm. The protrusion depth Δd_j and width l_o were chosen to be 1.36 μm and 5 μm, respectively. For this case, $l_o << \lambda_{max}$ = 31.4 μm as given by Eq. (2). The remaining parameter values are Ma = 9.69, Ca = 1.33 and u_c = 1.68 nm/s. The lateral feature size induced in the polymer film more closely approximates the imposed pattern width, which suggests that the ultimate resolution achievable by this method may require application of thermal gradients in close proximity to the polymer film.

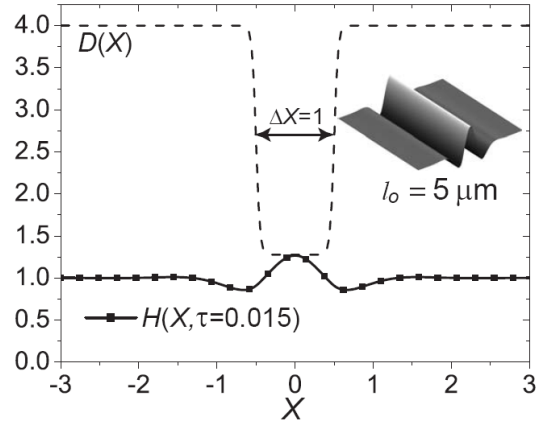

Figure 4 Film shape $H(X,\tau)$ induced by a ridge placed in close proximity to the polymer surface. The ridge width l_o is much smaller than the instability wavelength described by Eq. (2) pertinent to a flat wafer with no protrusions. Remaining parameter values are given in the text.

The differences in feature replication observed in Figures 2 – 4 are strongly dependent on the balance between thermocapillary and capillary terms in Eq.(1). This amplitude ratio is given by $\Psi = 3\kappa MaCa/[2(D+\kappa-1)^2]$ for deformations $\nabla_{\|} H$ of order 1. For the parameter values used in the studies shown in Figure 2, ψ=1.18. In Figure 3, ψ=18.9 for l_o=4 μm and ψ=29.6 for l_o=5 μm. In Figure 4, ψ=0.5. Good pattern replication is

therefore achieved for smaller values of ψ but a predominance of the term $\nabla_{\|} D$ in comparison to $\nabla_{\|} H$. This limit ensures that the imposed thermal gradient is set by the topology of the top wafer and not by the consequent deformations in film thickness *H*.

CONCLUSIONS

We have demonstrated by numerical simulation some features affecting pattern fidelity and waveform interference resulting from thermocapillary shaping of nanoscale polymer films. Selective growth of individual features is made possible in one process step despite the proximity of adjacent structure formation. Thermocapillary waves induced within the molten polymer film can be made to interfere constructively or destructively depending on the distance between emerging structures. This dynamic method of film patterning requires accurate temporal control to minimize feature distortion by thermocapillary waves.

ACKNOWLEDGMENTS

We gratefully acknowledge financial support for this study from the Electrical, Communications and Cyber Systems Division of the National Science Foundation.

REFERENCES

1. S. B. Fuller, E. J. Wilhelm and J. A. Jacobson, J. MEMS 11, 54 (2002).
2. S. M. Miller, S. M. Troian and S. Wagner, Appl. Phys. Lett. 83, 3207 (2003).
3. G. M. Gratson, M. J. Xu and J. A. Lewis, Nature 428, 386 (2004).
4. M. Heckele and W. K. Schomburg, J. Micromech. Microeng. 14, R1 (2004).
5. S. Y. Chou, P. R. Krauss and P. J. Renstrom, Appl. Phys. Lett. 67, 3114 (1995).
6. S. Y. Chou, L. Zhuang and L. J. Guo, Appl. Phys. Lett. 75, 1004 (1999).
7. E. Schäffer, S. Harkema, R. Blossey and U. Steiner, Europhys. Lett. 60, 255 (2002).
8. E. Schäffer, S. Harkema, M. Roerdink, R. Blossey and U. Steiner, Macromolecules 36, 1645 (2003).
9. E. Schäffer, S. Harkema, M. Roerdink, R. Blossey and U. Steiner, Adv. Mater. 15, 514 (2003).
10. J. Peng, H. F. Wang, B. Y. Li and Y. C. Han, Polymer 45, 8013 (2004).
11. M. Dietzel and S. M. Troian, arXiv:physics.flu-dyn http://arxiv.org/abs/0903.4899 (2009).
12. L.G. Leal, *Fluid Mechanics and Convective Transport Processes* (Cambridge University Press, NY, 2007).
13. COMSOL Multiphysics ® V3.4, Comsol, Inc. (Los Angeles, CA, 2007).
14. J. C. Moreira and N. R. Demarquette, J. Appl. Polym. Sci. 82, 1907 (2001).
15. J. L. Masson and P. F. Green, Phys. Rev. E 65, 31806 (2002).
16. D.R. Lide, *CRC Handbook of Chemistry and Physics*, 73rd ed. (CRC Publishing Co., Boca Raton, Fl. 1992).
17. J.E. Mark, *Physical Properties of Polymers Handbook*. (AIP Press, Woodbury, NY, 1996).